npj | precision oncology

Article

Published in partnership with The Hormel Institute, University of Minnesota

https://doi.org/10.1038/s41698-026-01389-y

IL-1-mediated inflammation promotes metastatic dissemination and resistance to EGFR-targeted therapy

Federica Pagano[1,10], Cinzia Girone[1,10], Francesco Borrelli[1], Donatella Romaniello[1,2], Valerio Gelfo[2], Daria Maria Filippini[2], Alessandra Morselli[1], Martina Mazzeschi[2], Giulia Querzoli[2], Francesca Ambrosi[1,3], Carmen Miano[2], Gabriele D'Uva[1,2], Francesco Fazi[4], Pradeep Chaluvally-Raghavan[5,6], Michela Sgarzi[2] ✉, Balazs Győrffy[7,8,9], Andrea Ardizzoni[2] & Mattia Lauriola[1,2] ✉

Resistance to anti-EGFR therapy remains a major challenge in head and neck squamous cell carcinoma (HNSCC), as adaptive mechanisms driven by drug-tolerant persister cells (DTPs) ultimately compromise treatment efficacy. Here, we identify Interleukin-1 (IL-1)-mediated inflammation as a critical driver of resistance to the anti-EGFR monoclonal antibody cetuximab (CTX). Through meta-analysis of HNSCC patient datasets stratified by lymph node status, together with in vitro studies using sensitive and CTX-resistant HNSCC cell lines and in vivo nude mouse models, we demonstrate that IL-1 in the tumor microenvironment reduces EGFR degradation, thereby promoting receptor stability and therapeutic escape. In sensitive cells, CTX suppresses the IL-1 pathway via direct transcriptional downregulation of IL-1α and IL-1β; however, this regulatory effect is lost in resistant cells, where a sustained IL-1-driven pro-inflammatory program enhances invadopodia formation, proliferation, and metastatic potential. Importantly, pharmacological inhibition of IL-1 in mice restored sensitivity to anti-EGFR therapy and prevented lung metastatic dissemination of resistant cells. These findings uncover an inflammatory axis underlying resistance and suggest that targeting IL-1 may improve EGFR-targeted therapies and limit metastatic spread in HNSCC.

Head and neck squamous cell carcinomas (HNSCCs) are a highly heterogeneous group of malignancies arising from the mucosal epithelium of the oral cavity, nasal cavity, pharynx, and larynx, with an annual incidence exceeding 500,000 cases worldwide[1].

The epidermal growth factor receptor (EGFR) has been found overexpressed in 80–90% of HNSCC tumors and is associated with poor clinical outcomes[2,3]. EGFR belongs to the tyrosine kinase receptor family and is part of a subclass of four receptors, ERBB1 (EGFR), ERBB2 (HER2), ERBB3 (HER3), and ERBB4 (HER4). Due to its frequent alterations, EGFR is also known as an oncogenic driver involved in the initiation and progression of head and neck cancer[4].

Cetuximab (CTX) is a monoclonal antibody (mAb) targeting EGFR, and it has been the first targeted drug approved by the FDA for recurrent/metastatic (R/M) disease and for the locally advanced setting, in combination with radiotherapy, as definitive treatment for platinum-unfit patients[5]. Recently, the therapeutic landscape in R/M setting has been rapidly evolving with the introduction of immune checkpoint inhibitors (ICIs), nivolumab and pembrolizumab[6,7]. Nevertheless, both anti-EGFR therapy and ICIs demonstrate limited efficacy, with only a minority of patients deriving clinical benefit and the mechanisms underlying inherent or acquired resistance need to be further elucidated.

[1]Department of Medical and Surgical Sciences, University of Bologna, Bologna, Italy. [2]IRCCS Azienda Ospedaliero-Universitaria di Bologna, Bologna, Italy. [3]Pathology Unit, Maggiore Hospital-AUSL Bologna, Bologna, Italy. [4]Department of Wellbeing, Health and Environmental Sustainability (BeSSA), Sapienza University of Rome, Rome, Italy. [5]Department of Obstetrics and Gynecology, Medical College of Wisconsin, Milwaukee, WI, USA. [6]Medical College of Wisconsin Cancer Center, Medical College of Wisconsin, Milwaukee, WI, USA. [7]Department of Bioinformatics, Semmelweis University, Budapest, Hungary. [8]Institute of Transdisciplinary Discoveries, Medical School, University of Pecs, Pecs, Hungary. [9]Cancer Biomarker Research Group, Institute of Molecular Life Sciences, HUN-REN Research Centre for Natural Sciences, Budapest, Hungary. [10]These authors contributed equally: Federica Pagano, Cinzia Girone. ✉e-mail: michela.sgarzi@aosp.bo.it; mattia.lauriola2@unibo.it

THE HORMEL INSTITUTE
UNIVERSITY OF MINNESOTA

Recent research is focusing on the combination of ICIs with anti-EGFR. Notably, a phase II trial that combined pembrolizumab with CTX achieved promising results with an overall response rate (ORR) of 45% at 6 months in patients with R/M HNSCC receiving first-line treatment[8].

We previously reported that in colorectal cancer, one of the mechanisms associated with the failure of EGFR neutralization by monoclonal antibodies involves the interplay between EGFR and IL-1 cytokines[9,10]. EGFR targeting leads to the activation of IL-1 with enhanced DNA damage and senescence, associated with a temporary cell cycle arrest, responsible for the acquisition of a drug-tolerant phenotype[11].

In line, there is an increasing association between HNSCC and chronic inflammation[12,13], and notably, IL-1/IL-1R signaling appears to play a key role[14]. IL-1α, IL-1β, the most studied ligands of the IL-1 family, and IL-1 receptor 1 (IL-1R1) were shown to be constitutively expressed in HNSCC[15–17]. IL-1α expression was also linked to enhanced tumor cell transmigration across the endothelium and to different pro-metastatic genes, including vascular endothelial growth factor (VEGF), matrix metalloproteinases (e.g., MMP-9), prostaglandin (PG) E_2, chemokine (e.g., CXCL8), and TGFβ[18]. Indeed, patients with distant metastasis displayed higher levels of secreted IL-1α than patients without metastasis, and increased expression of this cytokine has been related to an about 5-fold higher risk of developing metastasis[19]. Nevertheless, how the neutralization of IL-1 in combination with monoclonal antibodies targeting EGFR may dampen the migratory phenotype remains to be addressed.

Herein, we tested two HNSCC cell lines, FaDu and Cal-27, which under CTX treatment tend to downregulate both IL-1 α and β isoforms, while dramatically upregulating their receptor, IL-1R. In these cells, IL-1 secretion appears to decrease EGFR internalization and degradation and to drive the migratory phenotype of tumor cells unresponsive to CTX inhibition. Finally, in mice experiments, we showed that a combination of CTX with anti-IL-1 neutralizing molecules strikingly decreased the migratory capability of CTX-resistant cells.

Results

IL-1α and IL-1β levels are predictive of survival in lymph node–positive patients

Gene expression data derived from HNSCC RNA sequencing (RNA-seq) datasets were obtained from The Cancer Genome Atlas[20,21]. Within a reverse translational clinical trial framework (from bedside to bench), we performed a comprehensive analysis to investigate the association between IL-1α/β or IL-1R1 expression levels and overall survival (OS) in HNSCC. Cox proportional hazards regression was used to assess associations between gene expression and OS. Kaplan-Meier survival curves were generated to visualize survival differences. To evaluate the prognostic significance of IL-1α/β or IL-1R1, patient samples were stratified by the lower (T1) and upper (T3) expression terciles of the biomarker. A follow-up cutoff of 48 months was applied. The only analytical restriction involved the AJCC lymph-node status. Under this criterion, the dataset comprised 407 patients. No further filtering was applied; consequently, the analysis did not adjust for HPV status, smoking history, or treatment. In details, patients without distant metastatic lesions and lymph nodal involvement showed no difference in OS when stratified by higher or lower expression levels of IL-1α/β and IL-1R1, respectively, thereby excluding their role in tumor progression (Fig. 1A). On the contrary, differential expression levels of IL-1 α/β and IL-1R1 play a crucial role in determining the OS rate in patients with regional and distant lymph node metastases. Patients harboring regional lymph node positivity showed a considerable, yet not statistically significant, decrease in OS rate corresponding to high levels of IL-1 α/β. No trend was instead observed in the same category when IL-1R1 expression was analyzed (Fig. 1B). Strikingly, in patients with distant metastatic tumor lesions, a significant decrease in OS was observed in correlation with higher expression levels of IL-1 ligands, specifically IL-1α and IL-1β, consistent with the trend observed in the entire dataset. Here, increasing amounts of IL-1α and IL-1β severely impacted tumor patients' survival compared to lower expression levels of these ligands (Fig. 1C). Of note, no such difference with respect to the expression level of IL-1R1 corresponding to survival rate is noted in distant metastatic patients (Fig. 1C).

IL-1-driven inflammation limits CTX anti-invasive efficacy

Patient-derived data suggested that IL-1 signaling serves as a regulator in determining the OS in patients in a metastatic setting, hence, we analyzed the inhibition of the IL-1 cascade by employing anti-IL-1/IL-1R1 inhibitors alongside an anti-EGFR inhibitor to check the combinatorial drug efficacy in cellular proliferation. We employed two different inhibitors that specifically nullify the activity of IL-1α and IL-1R1 and evaluated their combined efficacy alongside CTX. Bermekimab (BMK) is an anti-IL-1α monoclonal antibody that specifically binds to soluble IL-1α, thereby neutralizing the cytokine-triggered signaling. Anakinra (ANA) (Kineret) is an anti-IL1R1 inhibitor that specifically binds to IL-1R1 as a decoy ligand with no biological activity, thus obstructing the potential binding of biologically active IL-1α/β to the receptor and inhibiting the ligand-receptor-mediated downstream signaling. We tested whether inhibitors targeting both IL-1 ligands and IL-1R1 could potentially enhance the efficacy of the anti-EGFR inhibitor, CTX, in two cancer cell lines (FaDu and Cal-27), which differ in their levels of IL-1R1 expression (Supplementary Fig. 1A). In a long-term (10 days) proliferation assay, CTX alone significantly reduced overall cell growth, with greater efficacy observed in FaDu cells. ANA alone did not produce any significant inhibitory effect in either cell line. In contrast, BMK alone exerted growth-inhibitory effects in FaDu cells; however, this effect was lost in Cal-27 cells (Fig. 2A, B). Importantly, the combination with IL-1/IL-1R1 inhibitors did not enhance the overall antiproliferative efficacy of CTX in both cell lines (Fig. 2A, B). Similar results were obtained in a 3-day experiment, showing a slight decrease in proliferation although not statistically significant, when IL-1 neutralizing antibody was combined with CTX (Supplementary Fig. 1B). CTX treatment also impacted on cell phenotype by enhancing cell thickness, while the combination with IL-1 neutralization rescued the untreated cells morphology (Supplementary Fig. 1C). Similar effects, although less striking, were detected on cell sphericity (Supplementary Fig. 1D). Notably, when testing cell motility, the instantaneous velocity of FaDu cells was statistically decreased in CTX combined with IL-1α neutralization (Fig. 2C), resulting also in a strong inhibition of persistent cell migration (Fig. 2D). Evaluation of FaDu cell invasion by gelatin degradation assays revealed that CTX significantly reduced invasive capacity, whereas BMK and ANA, when administered individually, did not exert a significant effect (Fig. 2E, F). These findings indicate that the reduction was primarily driven by CTX and not enhanced by the combination. In contrast, IL-1 α/β stimulation enhanced invasive capacity. Interestingly, the addition of BMK and ANA in combination with CTX under IL-1 α/β stimulation resulted in reduced invasion in both models (Fig. 2E–G), suggesting that IL-1 stimulation attenuated the anti-invasive effect of CTX.

An inflammatory microenvironment promotes EGFR stabilization

Next, we focused on the downstream targets of CTX inhibition. FaDu cells were treated with CTX in a time course over 96 h, which resulted in the downregulation of both EGFR phosphorylation and total EGFR levels, likely due to increased receptor degradation (Fig. 3A). Consistently, pAKT and pERK were also downregulated, although the effect on pAKT was more pronounced (Fig. 3A). Interestingly, IL-1R was upregulated as early as 24h after CTX treatment, both at the protein and mRNA levels (Fig. 3A, B). However, its ligands, IL-1α and β, along with IL-8 and IL-6 were consistently down-regulated by CTX (Fig. 3B), likely as a compensatory mechanism. CTX efficacy was also confirmed in Cal-27 by the late decrease of pEGFR levels (after 96 h), and its downstream effectors, pAKT and pERK, but total EGFR remained unchanged (Supplementary Fig. 2A). Notably, in this second model, CTX treatment induced the upregulation of IL-1R mRNA but the downregulation of IL-1R protein, along with IL-1α and β, IL-6 and IL-8 mRNAs (Supplementary Fig. 2B).

Following these observations, we employed a pHrodo-conjugated CTX and tracked the internalization of CTX to the acidic endosomal compartment with or without IL-1 in the microenvironment. We observed a

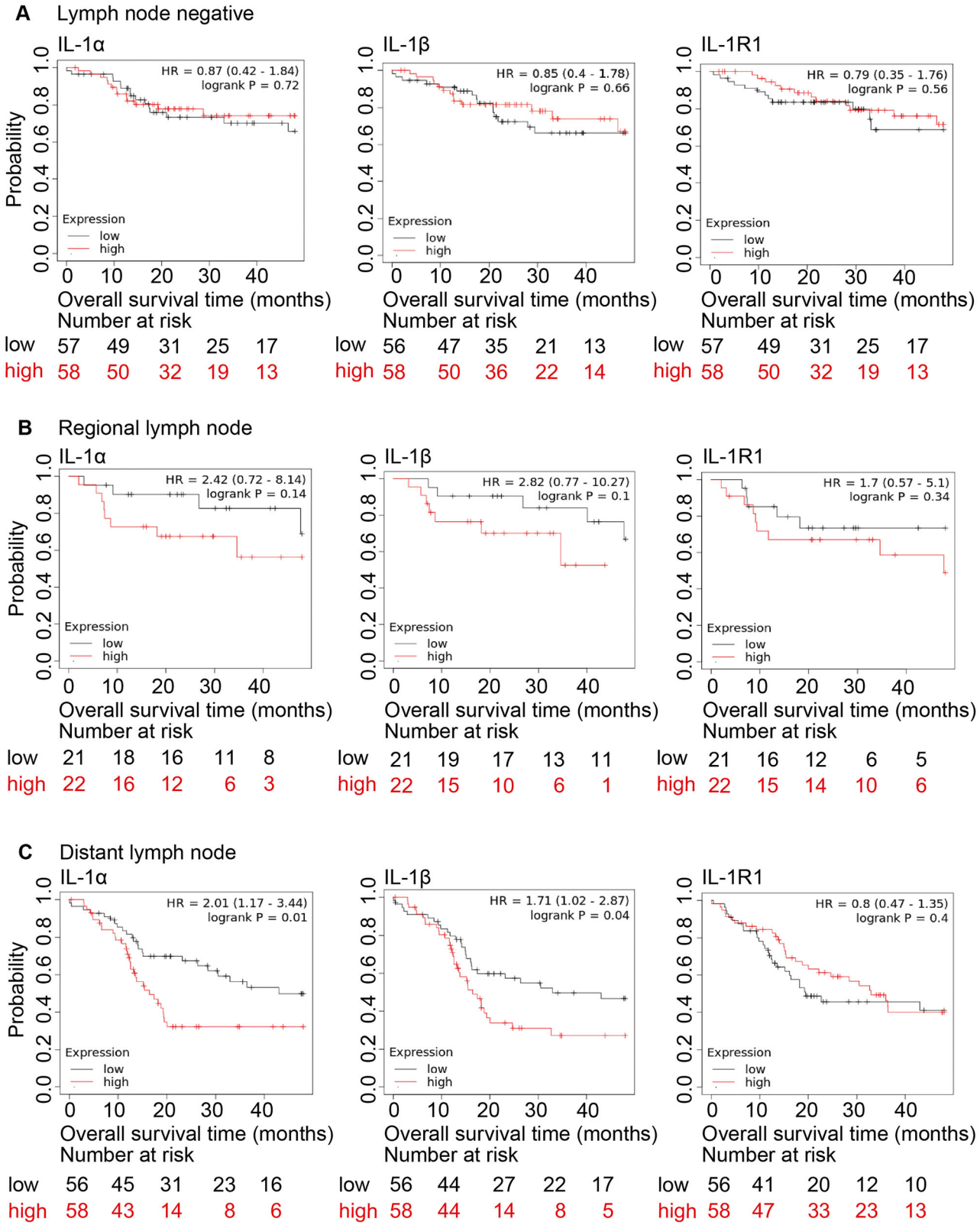

Fig. 1 | IL-1α and IL-1β are predictive of overall survival in HNSCC patients with distant lymph node metastases. A–C Kaplan–Meier analysis of a cohort of about 407 patients stratified by lymph node status and IL-1α, IL-1β, and IL-1R gene expression. The red line represents high level of expression, while the black one is representative of low levels. For each patient, the overall survival (OS) probability is reported over a period of more than 40 months. (**A**) lymph node negative, (**B**) regional lymph node, and (**C**) distant lymph node. *p*-value and hazard ratio (HR) are also presented.

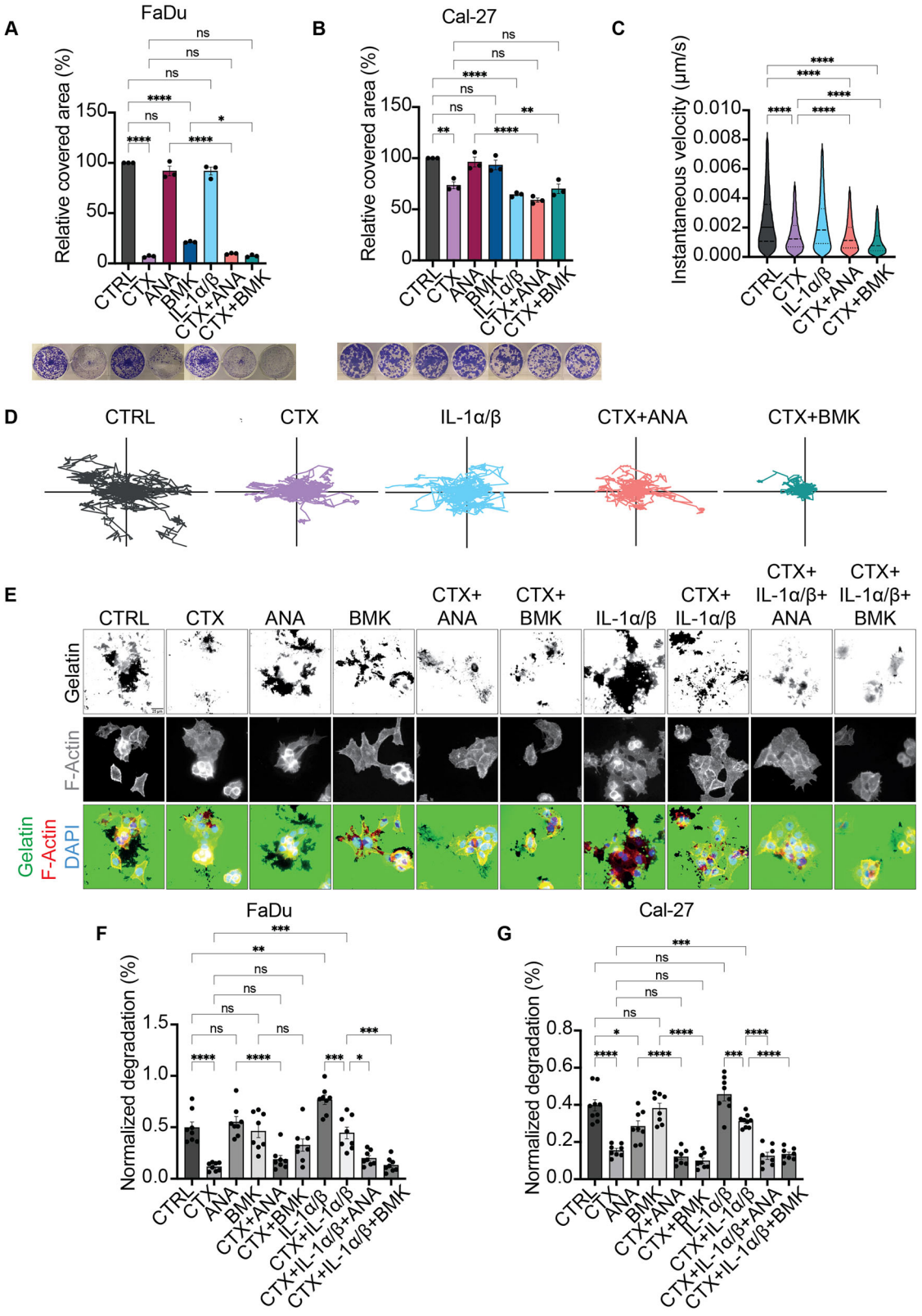

significant decrease in EGFR internalization when FaDu cells were treated with CTX in combination with IL-1, compared to CTX alone (Fig. 3C, D). Of note, IL-1 sequestration by ANA was able to restore CTX internalization level (Fig. 3C, D). Immunofluorescence analysis of membrane-associated EGFR showed a strong staining in untreated cells (Fig. 3E). Upon CTX treatment, EGFR level decreased, and localization was only evident in stress fiber-associated regions between adjacent cells. Interestingly, the addition of IL-1 to CTX appeared to counteract this redistribution, depicting EGFR decoration of the plasma membrane, consistent with the reduced internalization observed in the pHrodo assay (Fig. 3C, D). Finally, co-treatment with ANA partially restored the CTX-associated localization pattern of EGFR, with an overall decrease in signal intensity (Fig. 3E). Overall, these

Fig. 2 | CTX combined with IL-1 neutralization dampens cell invasion in IL-1-enriched microenvironment. A Colony forming assay of FaDu cell line treated with CTX (20 μg/mL), ANA (50 μg/mL), BMK (50 μg/mL) and their combination, and IL-1α/β (10 ng/mL each). Representative image of untreated and treated wells is shown. Cell viability data are reported as % of wells covered area in relation to controls ± SEM. Statistic was calculated by one-way ANOVA test. **B** Colony forming assay of Cal-27 cell line treated with CTX (50 μg/mL), ANA (50 μg/mL), BMK (50 μg/mL) and their combination, and IL-1α/β (10 ng/mL each). Representative image of untreated and treated wells is shown. Cell viability data are reported as % of wells covered area in relation to controls ± SEM. Statistic was calculated by one-way ANOVA test. **C** Measurement of instantaneous velocity of FaDu cells monitored for 72 h with Phasefocus LiveCyte™ platform. Cells were treated as in (**A**). Median and quartiles distribution are plotted. Outliers were identified and cleaned from results by means of ROUT method ($Q = 1\%$). Statistic was calculated by one-way ANOVA test. **D** Cell tracking from experiment in (**C**). A total of 50 cell tracks is reported. **E, F** Gelatin-degradation assay performed on FaDu cell line. Representative images, scale bar: 25 μm (**E**) and quantitative analysis of normalized degradation (**F**). Cells were treated with CTX (20 μg/mL), IL-1 α/β (10 ng/mL each), ANA (50 μg/mL), BMK (50 μg/mL) and their combination for 36 h. Cells were stained with Phalloidin-TRITC (F-Actin) and DAPI (nuclei) prior to visualization. Invasion was quantified in terms of the area of degraded gelatin (black spots visible in the green channel) normalized over the nuclei count in the same field. At least 8 fields were analyzed for each condition. Number of cells analyzed: CTRL: $n = 258$, CTX: $n = 182$, ANA: $n = 294$, BMK: $n = 221$, IL-1α/β: $n = 187$, CTX + ANA: $n = 164$, CTX + BMK: $n = 263$, CTX + IL-1α/β: $n = 234$, CTX + IL-1α/β + ANA: $n = 171$, CTX + IL-1α/β + BMK: $n = 189$. One-way ANOVA test was applied. **G** Gelatin-degradation assay performed on Cal-27 cell line treated with CTX (50 μg/mL), IL-1 a/b (10 ng/mL each), ANA (50 μg/mL), BMK (50 μg/mL) and their combination for 36 h. Cells were stained with Phalloidin-TRITC (F-Actin) and DAPI (nuclei) prior to visualization. Invasion was quantified as in (**F**). At least 8 fields were analyzed for each condition. Number of cells analyzed: CTRL: $n = 269$, CTX: $n = 263$, ANA: $n = 307$, BMK: $n = 253$, IL-1α/β: $n = 295$, CTX + ANA: $n = 349$, CTX + BMK: $n = 300$, CTX + IL-1α/β: $n = 302$, CTX + IL-1α/β + ANA: $n = 297$, CTX + IL-1α/β + BMK: $n = 385$. One-way ANOVA test was applied.

data suggest that an inflammatory microenvironment could alter EGFR trafficking, counteracting CTX-induced EGFR internalization.

IL-1 neutralization inhibits the migratory behavior of CTX-resistant cells

The efficacy of CTX has traditionally been attributed to its ability to inhibit cell growth. However, systemic anticancer therapies may promote the emergence of drug-tolerant persister (DTP) cells within tumors that initially respond to treatment[22]. Therefore, we tested whether DTPs arise under CTX treatment. Indeed, drug-tolerant cells that were able to grow in the presence of CTX regained their sensitivity to the drug once it was removed. Notably, both ANA and BMK further enhanced the efficacy of CTX in these CTX-DTPs (Fig. 4A). Finally, we developed a model of cetuximab-resistant (CXR) cells by exposing cells to gradually increasing concentrations of CTX, ranging from 100 ng/mL to 20 μg/mL for FaDu and 50 μg/mL for Cal-27. The cells' ability to proliferate over 10 days under CTX treatment was evaluated based on their capacity to cover the available surface area. CTX-R cells exhibited dependency on continuous CTX exposure, as withdrawal of CTX resulted in a significant reduction in the proliferative capacity (Fig. 4B), whereas adding ANA or BMK to CTX only mildly reduced cell proliferation (Fig. 4C and Supplementary Fig. 2C). Similar results were observed over a 72-h period when normalized cell counts were analyzed. Specifically, FaDu-CXR cells exhibited exponential growth under CTX treatment, confirming the acquisition of resistance, and the combination with ANA or BMK dampened this effect (Supplementary Fig. 2D). However, this was not repeated in Cal-27 CXR cells (Supplementary Fig. 2E).

The most compelling results were obtained by assessing the migratory behavior of FaDu-CXR cells. Using time-lapse imaging to track cell movement, we observed a significant reduction in the mean velocity of CTX-resistant cells when ANA or BMK were combined to CTX treatment (Supplementary Fig. 2F). Specifically, the instantaneous velocity of cells treated with the combination was reduced by half compared to CTX treatment alone (Fig. 4D). Moreover, the directional migration of the cells was dramatically impaired in the presence of the combination therapy, as evidenced by a marked reduction in migration efficiency and persistence (Fig. 4E). Instantaneous velocity reduction was also detected in Cal-27 CTX-R cells treated with CTX plus IL-1 inhibitors (Supplementary Fig. 2G).

These findings underscore the selective ability of ANA and BMK to significantly suppress the migratory and invasive behavior of CXR cells, which are pivotal for tumor progression and metastasis, whereas their impact on cell proliferation was less pronounced.

The ability of cells to grow in a 3D system, which more closely mimics the in vivo tumor microenvironment, was also assessed in both parental and resistant cell lines. FaDu spheroids displayed a well-organized architecture, characterized by a stratified epithelial layer surrounding a central cavity. Cells exhibited strong intercellular adhesion, as demonstrated by robust membrane E-cadherin expression, and showed no evidence of epithelial-mesenchymal transition (EMT), as indicated by the absence of vimentin expression (Supplementary Fig. 3A, above). Ki-67 staining confirmed a high proliferative index within the spheroids (Supplementary Fig. 3A, above). CXR cells also formed spheroids in 3D culture; however, their structural organization differed from that of parental FaDu cells. CXR spheroids tended to fill the central cavity, resulting in a markedly thicker epithelial layer (Supplementary Fig. 3A, below). This phenotype suggests an increased ability of resistant cells to evade anoikis and survive under nutrient-deprived conditions, allowing proliferation within the inner spheroid regions. Despite these architectural differences, CXR spheroids maintained epithelial features, including preserved membrane E-cadherin expression and absence of vimentin (Supplementary Fig. 3A, below). Ki-67 staining further confirmed sustained proliferative activity. Overall, while both cell lines retained epithelial characteristics and high proliferative capacity in 3D culture, CXR spheroids exhibited a more compact, cavity-filling architecture, potentially reflecting enhanced adaptive and survival mechanisms.

In contrast to the 2D proliferation assays, CTX treatment exerted only a mild inhibitory effect on spheroid growth over the 4-day experimental period. Moreover, the combination of CTX with ANA or BMK did not significantly enhance this effect (Supplementary Fig. 3B). The limited efficacy of CTX combined with IL-1 neutralization in blocking tumor growth is in line with previous in vivo studies performed in mice bearing Cal-27 tumors[23]. Conversely, CXR spheroids, which are maintained under continuous CTX exposure, showed a significant reduction in spheroid size upon the addition of ANA or BMK (Supplementary Fig. 3C), suggesting that IL-1 inhibition exerts a measurable impact specifically in the resistant setting.

IL-1 neutralization alters EGFR trafficking in CTX-resistant cells

We next evaluated the mRNA levels of a panel of inflammatory cytokines, including IL-1 α, IL-1β, and their receptor IL-1R. In sensitive cells, these cytokines were significantly downregulated under both CTX treatment and the combination with ANA and BMK, compared to untreated condition (Fig. 5A). Interestingly, IL-1R levels were upregulated under the combination treatment with ANA and BMK (Fig. 5A). In contrast, resistant cells grown in CTX displayed a striking increase in these cytokines, with IL-1α and IL-1β levels being approximately 7-fold and 4-fold higher, respectively, compared to sensitive cells treated with the drug (Fig. 5A). However, this elevated expression was sustained even with the combination treatments involving BMK or ANA, which instead were successfully able to decrease the expression of the EMT marker SNAI (Fig. 5A).

Finally, in the context of CTX resistance, we tested the level of EGFR internalization under CTX and IL-1R1 neutralization. Apparently, when treated with the combination of CTX plus ANA, resistant cells exhibited a strong increase in CTX internalization compared to CTX alone after 48 h of treatment (Fig. 5B, C). To determine whether this enhanced internalization

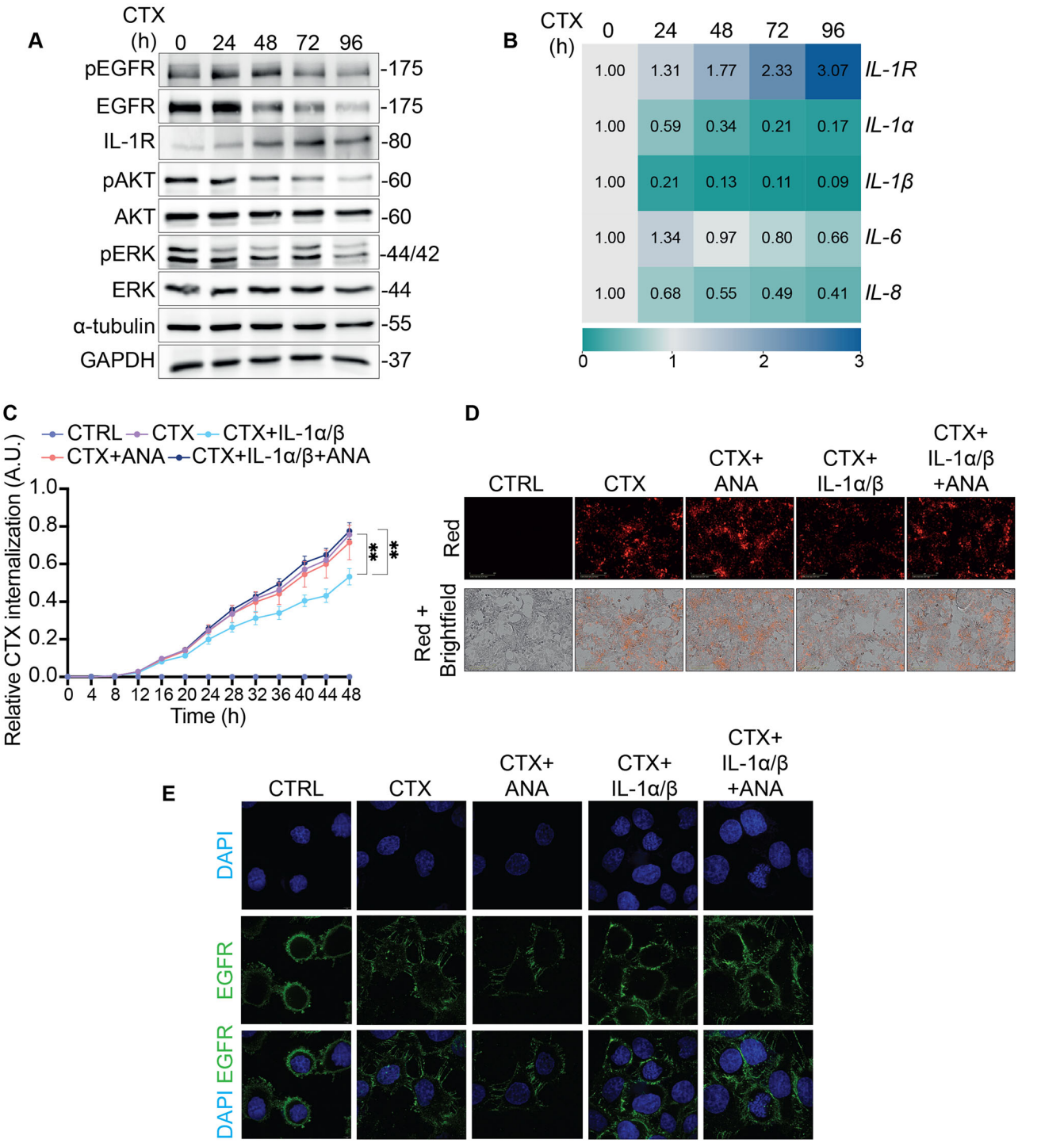

Fig. 3 | IL-1 driven inflammation hampers EGFR internalization. A Protein analysis of EGFR signaling pathway in FaDu cells treated with CTX (20 μg/mL) over a 96 h time course. The blots for pEGFR, EGFR, pAKT, and AKT belong to the same membrane and GAPDH was used as loading control. Similarly, IL-1R, pERK, and ERK belong to the same membrane and α-tubulin was used as loading control. **B** Heatmap depicting mRNA levels of pro-inflammatory cytokines expression by qPCR analysis performed on FaDu cells treated as in (**A**). B2M was used as housekeeping gene for normalization. **C, D** pHrodo™ Red-labeled CTX internalization in FaDu cells. Quantification of relative CTX internalization (A.U.) (**C**) and representative images, scale bar: 200 μm (**D**). Cells were treated with pHrodo-labeled CTX (1 μg/mL), IL-1α/β (10 ng/mL each), ANA (50 μg/mL) and their combination. Red fluorescent channel and brightfield images were acquired every 4 h (for 48 h). The internalization index (arbitrary units, A.U.) was calculated over 48 h as ratio of trafficking index and the Imax (maximum intensity value of CTX red channel) using live-cell imaging. Data are presented as mean ± SEM and statistic was calculated with two-way ANOVA with multiple comparisons. **E** Immunofluorescence assay performed on FaDu cells treated as in (**C**) but with CTX (20 μg/mL). Cells were stained with EGFR (green) and DAPI (nuclei) prior to visualization. Images were acquired as Z-stacks using IXplore IX83 SpinSR spinning disk confocal microscope (Olympus/Evident) and are presented as maximum intensity projections of the acquired stacks. Scale bar: 5 μm.

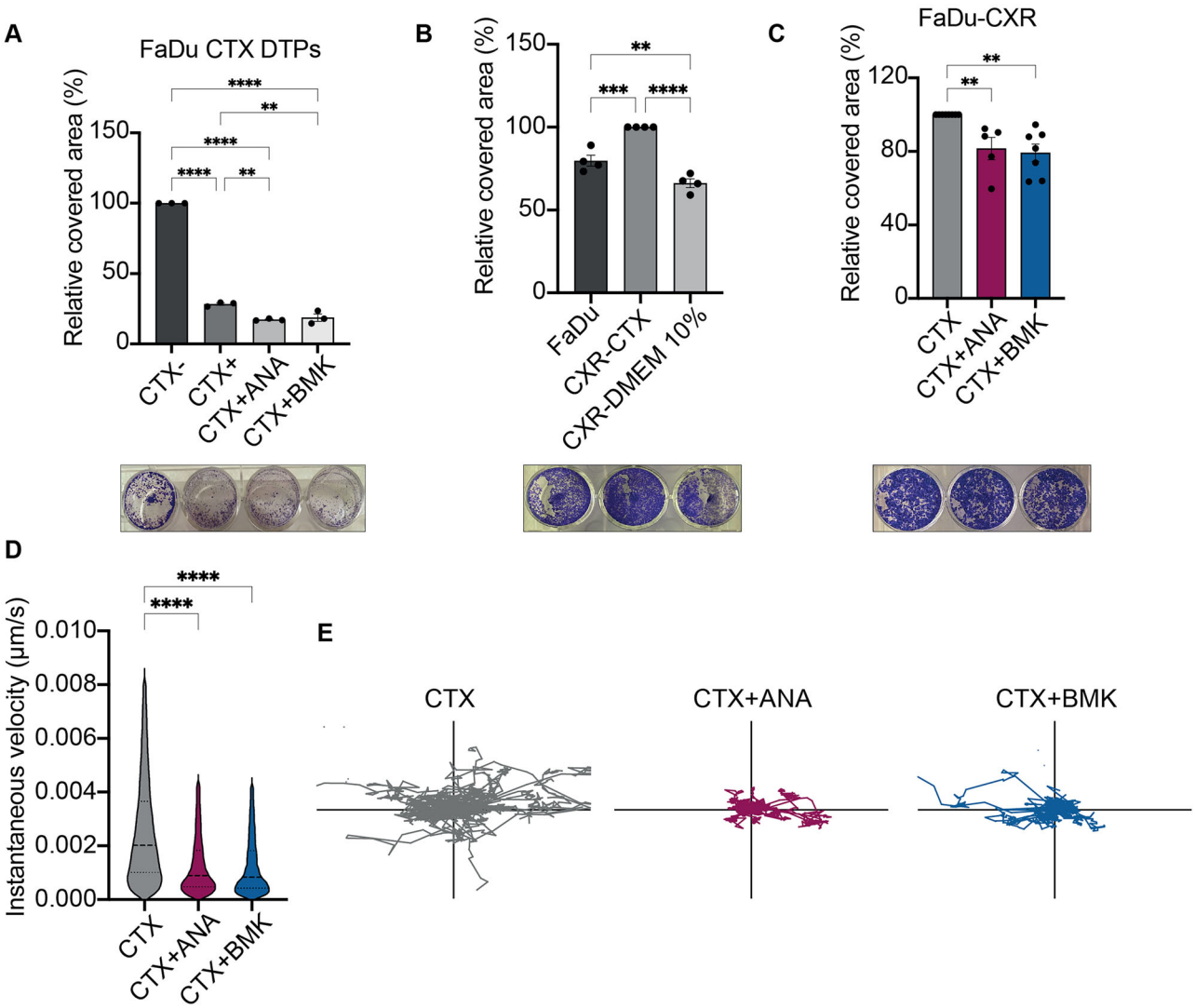

Fig. 4 | IL-1 neutralization inhibits cells migration in CTX-resistant cells. **A** Colony-forming assay of FaDu CTX DTPs treated with CTX (50 µg/mL), ANA (50 µg/mL) and BMK (50 µg/mL). Representative image of treated wells is shown. Cell viability data are reported as % of wells covered area in relation to controls ± SEM. Statistic was calculated by one-way ANOVA test. **B** Colony-forming assay of FaDu and FaDu-CXR cell line growing in CTX (20 µg/mL), or CTX withdrawal. Representative image of treated wells is shown. Cell viability data are reported as in (**A**). Statistic was calculated by one-way ANOVA test. **C** Colony forming assay of FaDu-CXR cell line growing in CTX (20 µg/mL) and treated with ANA (50 µg/mL) and BMK (50 µg/mL). Representative image of treated wells is shown. Cell viability data are reported as % of wells covered area in relation to controls ± SEM between two independent experiments. Statistic was calculated by one-way ANOVA test. **D** Measurement of instantaneous velocity of FaDu-CXR cells monitored for 72 h with Phasefocus LiveCyte™ platform. Cells were treated as in (**C**). Median and quartiles distribution are plotted. Outliers were identified and cleaned from results by means of ROUT method ($Q = 1\%$). Statistic was calculated by one-way ANOVA test. **E** Cell tracking from experiment in (**D**). A total of 50 cell tracks is reported.

resulted in receptor degradation, we evaluated EGFR protein levels. Surprisingly, total EGFR levels were markedly increased in the CTX + ANA condition and only slightly increased with CTX + BMK (Fig. 5D). Notably, IF imaging confirmed these findings, showing enhanced EGFR accumulation at the plasma membrane in the CTX + ANA condition (Fig. 5E). This indicates that, despite enhanced internalization, EGFR is not efficiently directed toward degradation. Likely, IL-1 neutralization altered trafficking dynamics, potentially favoring receptor recycling or impaired degradative routing.

CTX-resistant cells show enhanced DNA damage responses

Next, we investigated whether CTX therapy induces the expression of error-prone DNA polymerases. Interestingly, CTX exposure in parental cells was associated with a reduced DNA repair fidelity, characterized by a shift from high-fidelity to low-fidelity DNA polymerases. Polymerases involved in accurate DNA replication, including POLδ, POLα, and POLε, were downregulated after 48 h of CTX treatment. In contrast, error-prone polymerases lacking proofreading activity, such as POLι, POLλ, POLμ, POLκ and REV1, were upregulated (Fig. 6A). These findings are consistent with previous observations reported by Russo et al. in colorectal cancer models[24]. We then evaluated whether IL-1α and IL-1β stimulation could similarly promote genomic instability in sensitive cells and favor error-prone DNA repair. Indeed, IL-1 treatment significantly induced low-fidelity polymerases (POLι, POLλ, POLκ, and REV1), while high-fidelity polymerases (POLδ, POLα, and POLε) were downregulated (Fig. 6A). These data indicate that a pro-inflammatory environment promotes a shift toward error-prone DNA damage repair, potentially increasing the likelihood of mutations associated with drug resistance. IL-1 neutralization with ANA alone slightly increased the expression of low-fidelity polymerases. However, after 48 h, the combination of CTX and ANA attenuated the CTX-

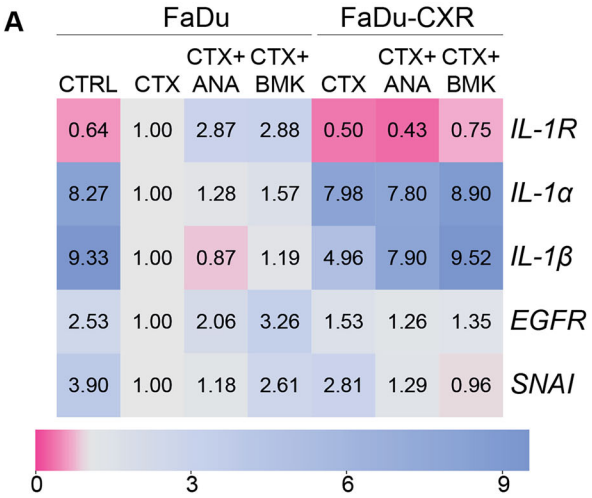

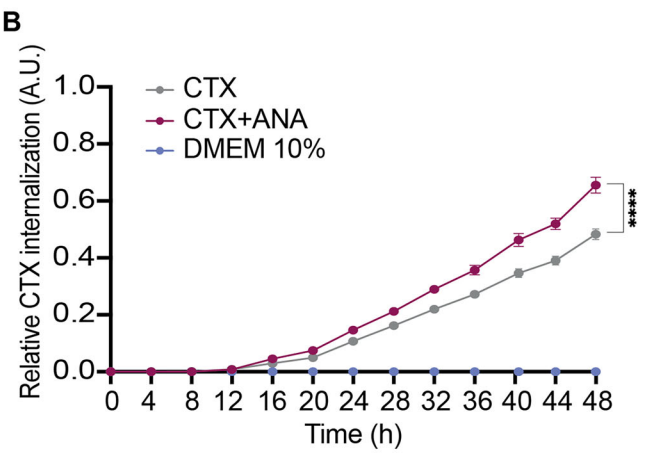

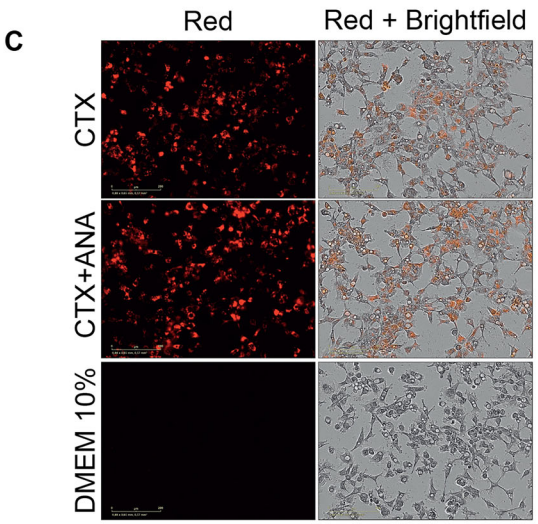

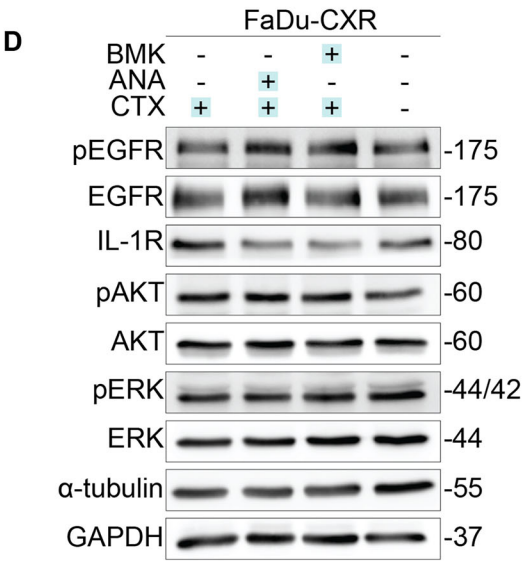

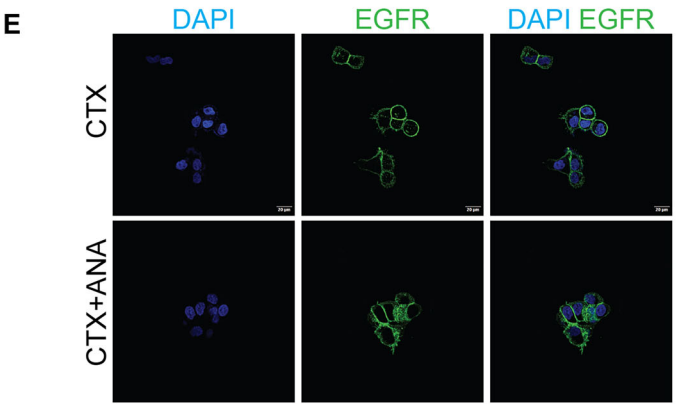

induced upregulation of these genes. Notably, this attenuation was partially reversed upon exogenous IL-1 addition to CTX + ANA treatment (Fig. 6A).

To further explore the potential functional consequences of these alterations, we assessed γH2AX foci formation over time as a marker of DNA damage. In parental cells, 48 h of CTX treatment did not lead to a significant increase in γH2AX foci (Fig. 6B, C), suggesting that either prolonged exposure is required to detectable DNA damage or that the transcriptional reprogramming of DNA polymerases does not immediately translate into measurable genomic stress. Similarly, the combination of CTX + ANA did not significantly alter γH2AX level at this time point. On the other hand, CTX-resistant cells exhibited higher baseline levels of DNA damage, with approximately a twofold increase in γH2AX foci compared to sensitive cells. Interestingly, IL-1 neutralization with ANA further enhanced DNA damage accumulation (Fig. 6B, C).

Fig. 5 | IL-1 blockade modulates EGFR trafficking in CTX-resistant cells. **A** Heatmap depicting mRNA levels of IL-1R, IL-1α, IL-1β, EGFR, and SNAI expression by qPCR analysis performed on FaDu and FaDu-CXR cell lines. FaDu cells were treated with CTX (20 μg/mL), ANA (50 μg/mL) and BMK (50 μg/mL), and their combination. FaDu-CXR cells were grown in CTX (20 μg/mL) and treated with ANA (50 μg/mL) and BMK (50 μg/mL) for 96 h. B2M was used as a house-keeping gene for normalization. **B, C** pHrodo™ Red-labeled CTX internalization in FaDu-CXR cells. Quantification of relative CTX internalization (A.U.) (**B**) and representative images, scale bar: 200 μm (**C**). Cells were treated with pHrodo-labeled CTX (1 μg/mL), alone or in combination with ANA (50 μg/mL) Red fluorescent channel and brightfield images were acquired every 4 h (for 48 h). The internalization index (arbitrary units, A.U.) was calculated over 48 h as ratio of trafficking index and the Imax (maximum intensity value of CTX red channel) using live-cell imaging. Data are presented as mean ± SEM and statistic was calculated with two-way ANOVA with multiple comparisons. **D** Protein analysis of EGFR signaling pathway and IL-1R in FaDu-CXR cells maintained in CTX (20 μg/mL) and treated with ANA (50 μg/mL), BMK (50 μg/mL) or CTX withdrawal for 48 h. The blots for pEGFR, EGFR, pAKT, and AKT belong to the same membrane and GAPDH was used as loading control. Similarly, IL-1R, pERK, and ERK belong to the same membrane and α-tubulin was used as loading control. **E** Immunofluorescence assay performed on FaDu-CXR cells growing in CTX (20 μg/mL) and treated with ANA (50 μg/mL) for 48 h. Cells were stained with EGFR (green) and DAPI (nuclei) prior to visualization. Images were acquired as Z-stacks using IXplore IX83 SpinSR spinning disk confocal microscope (Olympus/Evident) and are presented as maximum intensity projections of the acquired stacks. Scale bar: 20 μm.

These results were repeated in 3D spheroid models. Notably, parental spheroids treated with CTX for 96 h exhibited a significant increase in γH2AX foci compared to untreated controls (Supplementary Fig. 3D, E), indicating that prolonged drug exposure in the 3D context results in detectable DNA damage. Consistent with the 2D findings, CTX-R spheroids showed a significantly higher number of γH2AX foci per cell compared to parental spheroids (Supplementary Fig. 3D, E). Taken together, these data indicate that CTX resistance is associated with elevated baseline genomic instability, which is further exacerbated by IL-1 neutralization. Although the precise functional consequences of this interaction remain to be elucidated, these findings suggest a potential link between inflammatory signaling, adaptive DNA repair mechanisms, and resistance-associated genomic stress.

IL-1 neutralization decreases cell invasion in CTX-resistant cells

The data collected so far strongly suggest that dual targeting with CTX and IL-1 neutralization may affect cell migration, leading to a significant inhibition of persistent cell movement. These findings are consistent with patient-derived data, which highlight a critical role for IL-1 in promoting distant metastasis. To further investigate this mechanism, we performed an invadopodia-based invasion assay, quantifying gelatin matrix degradation in the resistant setting. We employed both CTX-resistant cell models: FaDu-CXR cells and Cal-27-CXR. In FaDu-CXR cells, the combination of CTX with IL-1 inhibitors (either ANA or BMK) led to a statistically significant reduction in the invasive capacity (Fig. 7A, B). In contrast, in Cal-27-CXR cells, a significant decrease in invasion was observed only with the CTX + BMK combination (Fig. 7C, D).

Finally, we performed in vivo experiments to evaluate the efficacy of IL-1 inhibition in controlling lung metastasis of CTX-resistant FaDu cells. As described above, in the resistant setting, FaDu-CXR cells are continuously maintained in the presence of CTX, reflecting their acquired drug-adapted phenotype and modeling the clinical scenario in which patients continue CTX therapy despite disease progression. Based on this rationale, FaDu-CXR cells were injected into the tail vein of mice, which were then treated with CTX alone or in combination with ANA. Consistent with the in vitro design, CTX administration was maintained throughout the in vivo study to preserve the resistant context. After six weeks, mice were sacrificed, and lungs were collected for histopathology and gene expression analysis (Fig. 7E). Lung colonization was evaluated by measuring the ratio between human EGFR (*hEGFR*), which is specific to the cancer cells, and murine *Gapdh* (*mGapdh*). These two targets showed no cross-amplification, allowing highly sensitive qPCR analysis to detect even minimal seeding of FaDu-CXR cells in the lungs.

Notably, CXR cells successfully disseminated to the lungs of all mice (8 out of 8) treated with CTX and showed detectable expression of hEGFR. Four of the eight mice exhibited markedly elevated expression, with fold-change values ranging approximately from 600 to 1400 relative to the negative control (Fig. 7F). In contrast, the combination with ANA completely abolished the ability of FaDu CXR cells to invade the lungs: 5 out of 9 mice were completely negative for hEGFR expression, and 3 mice presented almost negligible levels of hEGFR and only one with a detectable ~130-fold. (Fig. 7F). Strikingly, these data were repeated in a second experiment in which mice were treated similarly for four weeks; indeed 5 out 6 mice treated with CTX showed positive hEGFR expression, while 7 out of 7 mice treated with CTX + ANA were negative (Supplementary Fig. 4).

To further confirm the formation of lung metastatic lesions, hematoxylin-eosin and cytokeratin 14 (CK14) staining were performed. In mice treated with CTX alone, extensive metastatic deposits were observed, consisting of solid nests and lobules of basaloid squamous carcinoma showing peripheral palisading, characterized by cells aligned in a fence-like arrangement, and central necrosis (Fig. 7G). Tumor cells exhibited a high nuclear-to-cytoplasmic ratio, scant and indistinct cytoplasm lacking intercellular bridges, and minimal keratinization, consistent with a basaloid morphology. Numerous mitotic figures, including atypical forms, and apoptotic bodies were readily identified. Immunohistochemically, tumor cells displayed strong, diffuse cytoplasmic and membranous CK14 expression (Fig. 7G). In contrast, lungs from mice receiving CTX + ANA showed preserved alveolar architecture and a complete absence of CK14 immunoreactivity, indicating the lack of disseminated tumor cells (Fig. 7G). Taken together, these results strongly support a causative role for IL-1 in driving metastatic spreading and suggest that a combinatorial therapy approach of IL-1 inhibition with CTX could be effective in preventing progression toward metastatic disease.

Discussion

The heterogeneity of the tumor microenvironment (TME) in HNSCC represents one of the barriers to therapeutic efficacy[25]. In this context, HNSCC tissue samples positively scored for IL-1α were reported to display a perineural invasion and were significantly associated with a high risk of tumor recurrence[26]. Recent single-cell computational analyses of the immune infiltrate in human HNSCC have identified a distinct subpopulation of regulatory T (Treg) cells enriched within tumors but absent in healthy inflamed tissues, characterized by co-expression of ICOS and IL-1R1[27]. Given the well-established role of Treg cells in suppressing anti-tumor immunity, this subset may represent a tumor-specific immunosuppressive population. In this context, tumor-derived IL-1 could selectively activate IL-1R1$^+$ Treg cells, thereby dampening immune responses and facilitating metastatic dissemination[27]. Considering the modest clinical response rates achieved with pembrolizumab (16–18%) or cetuximab (6–13%) as monotherapies[28], our data provide a strong rationale for therapeutic strategies combining EGFR-targeting monoclonal antibodies downregulating tumor IL-1, with immune checkpoint inhibitors, particularly in tumors characterized by an IL-1-driven immunosuppressive microenvironment. Nevertheless, further studies are required to optimize patient stratification to identify those most likely to benefit from such combinatorial approaches. Notably, both the present study and the work cited above rely primarily on the assessment of IL-1 mRNA expression. This may appear at odds with previous reports showing that EGFR inhibition by TKIs or monoclonal antibodies induces the release of pro-inflammatory cytokines, including IL-1α, IL-6, and IL-8[23,29]. However, since dynamic analyses of mRNA expression were not performed over time, we cannot exclude the possibility that the reported cytokine release reflects secondary

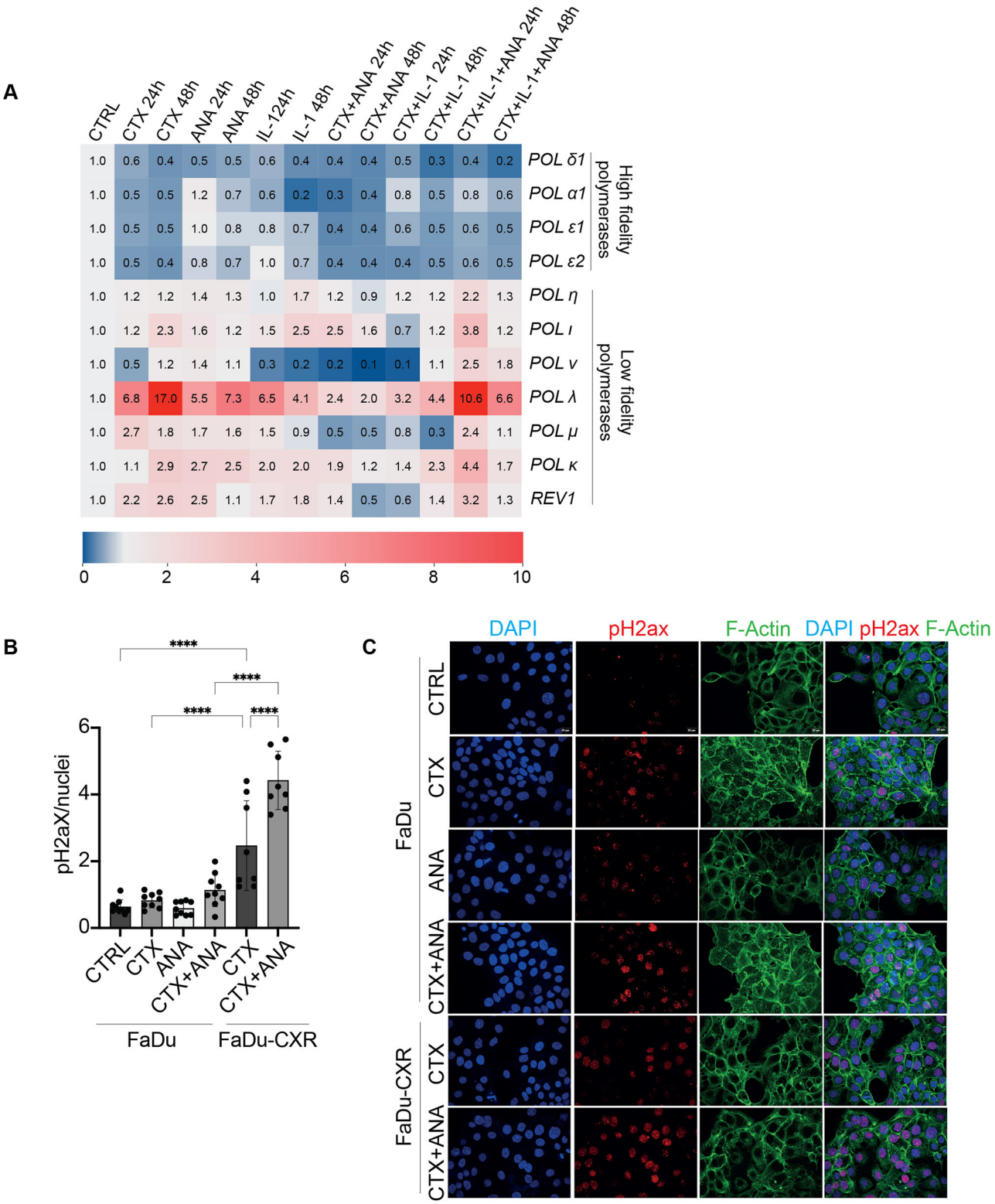

Fig. 6 | CTX resistance associates with increased DNA damage response. **A** Heatmap depicting mRNA levels of high/low fidelity polymerases by qPCR analysis performed on FaDu cells treated with CTX (20 μg/mL), ANA (50 μg/mL), IL-1α/β (10 ng/mL each) and their combination in the indicated time points. B2M was used as housekeeping gene for normalization. **B, C** Immunofluorescence assay performed on FaDu and FaDu-CXR cell lines. FaDu cells were treated with CTX (20 μg/mL), ANA (50 μg/mL) and their combination for 48 h. FaDu-CXR cells were grown in CTX (20 μg/mL) and treated with ANA (50 μg/mL) for 48 h. Cells were stained with pH2ax (red), Phalloidin-FITC (F-Actin) and DAPI (nuclei) prior to visualization. Foci count was normalized over the nuclei. At least 8 fields were analyzed for each condition. Number of FaDu cells analyzed: CTRL: $n = 966$ CTX: $n = 824$, ANA: $n = 907$, CTX + ANA: $n = 964$. Number of FaDu-CXR cells analyzed: CTX: $n = 535$, CTX + ANA $n = 408$. Data are reported as mean ± SEM. Statistic was calculated by one-way ANOVA. Representative images were acquired as Z-stacks using IXplore IX83 SpinSR spinning disk confocal microscope (Olympus/Evident) and are presented as maximum intensity projections of the acquired stacks (**C**). Scale bar: 20 μm.

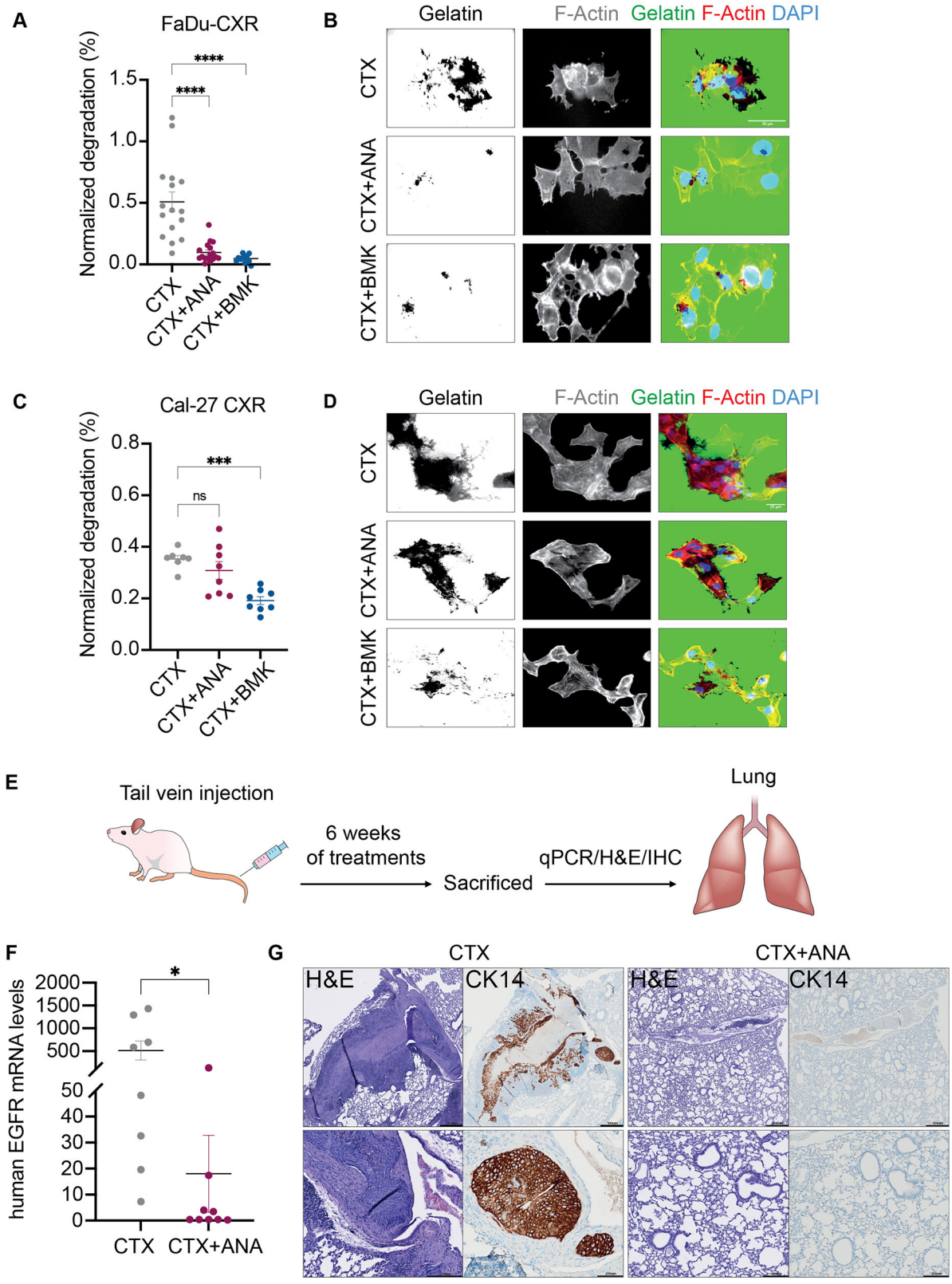

effects of drug-induced cell death rather than sustained transcriptional activation.

Our clinical data align with previous findings showing that patients with high tumor expression of IL-1α and IL-1β had significantly poorer overall survival[30] and support the notion that IL-1α/β expression may serve as a potential prognostic biomarker in HNSCC, warranting validation in larger, prospectively characterized cohorts. We observed that IL-1 expression positively correlates with the acquisition of resistance to cetuximab, as also reported in erlotinib-resistant HNSCC models[31]. This may reflect an adaptive mutational state[32], whereby, as resistance develops, tumors become dependent on these cytokines, potentially contributing to the accumulation of DNA damage. Indeed, the secretion of inflammatory cytokines may

Fig. 7 | IL-1 neutralization counters cell invasion under CTX resistance. A, B Gelatin-degradation assay performed on FaDu-CXR cell line. Quantitative analysis of normalized degradation (**A**) and representative images, scale bar: 50 µm (**B**). Cells were grown in CTX (20 µg/mL) and treated with ANA (50 µg/mL) and BMK (50 µg/mL) for 36 h. Cells were stained with Phalloidin-TRITC (F-Actin) and DAPI (nuclei) prior to visualization. Invasion was quantified in terms of area of degraded gelatin (black spots visible in the green channel) normalized over the nuclei count in the same field. At least 14 fields were analyzed for each condition. Number of cells analyzed: CTX: $n = 243$, CTX + ANA: $n = 342$, CTX + BMK: $n = 280$. Outliers were identified and cleaned from results by means of ROUT method ($Q = 1\%$). One-way ANOVA test was applied. **C, D** Gelatin-degradation assay performed on Cal-27 CXR cell line. Quantitative analysis of normalized degradation (**C**) and representative images, scale bar: 25 µm (**D**). Cells were grown in CTX (50 µg/mL) and treated with ANA (50 µg/mL) and BMK (50 µg/mL) for 36 h. Cells were stained with Phalloidin-TRITC (F-Actin) and DAPI (nuclei) prior to visualization. Invasion was quantified as in (**A**). At least 8 fields were analyzed for each condition. Number of cells analyzed: CTX: $n = 207$, CTX + ANA: $n = 213$, CTX + BMK: $n = 225$. Outliers were identified and cleaned from results by means of ROUT method ($Q = 1\%$). One-way ANOVA test was applied. **E** Distant lung metastatic model established via tail vein injection of FaDu-CXR cell line grown in CTX (20 µg/mL). Mice were treated with CTX alone (100 mg/injection) or in combination with ANA (10 mg/kg). **F** Determination of human EGFR by qPCR analysis performed on mouse lungs from experiment in (**E**). Mouse GAPDH was used as housekeeping gene for normalization. Two tailed unpaired T- test was applied for statistical analysis. **G** Representative H&E and CK14 staining of mouse lungs from experiment in (**E**). Scale bar: 500 µm (above), 200 µm (below).

impact DNA damage[33–35]. Specifically, EGFR neutralization induces alterations in DNA repair mechanisms, characterized by the downregulation of high-fidelity polymerases and the concurrent upregulation of low-fidelity polymerases, increasing the likelihood of developing resistant clones, ultimately leading to therapy failure[36,37].

One of the most compelling findings of this study is understanding how IL-1 signaling may impact HNSCC tumor response to CTX. Previous studies in both immunodeficient and immunocompetent mouse models have shown that administration of ANA does not enhance the anti- proliferative effect of CTX[27]. Consistent with these reports, our results indicate that the combination of CTX and ANA does not significantly reduce proliferation. However, we observed that this combination effectively inhibits migration and invasion, suggesting that IL-1 blockade may play a critical role in limiting metastatic spread, similarly to the effects reported with selective COX-1 inhibitors[38]. Moreover, the possible implication of this drug's immunomodulatory effect remains to be fully explored. This is particularly relevant considering recent evidence indicating that common viral respiratory infections can awaken dormant cancer cells in the lungs, promoting the formation of new metastatic lesions through activation of IL-6[39]. If confirmed in additional models, targeting this pathway could limit cancer cell dissemination and improve patient survival, representing a promising therapeutic strategy.

Finally, we highlight a role for inflammation in modulating EGFR trafficking and degradation. Specifically, IL-1α/β reduces EGFR internalization and degradation in CTX-sensitive cells. In contrast, in resistant cells, CTX fails to efficiently direct EGFR toward degradation. Overall, our work characterizes multiple mechanisms by which a pro-inflammatory microenvironment can modulate the response to CTX and metastatic potential in HNSCC. In this perspective, our data support the rationale for investigating a combinatorial strategy based on IL-1 neutralization in combination with CTX in advanced HNSCC.

Methods

Patient analyses

All patient data processing and statistical analyses were conducted in the R statistical environment (v3.5.2; http://www.r-project.org). HNSCC sequencing (RNA-seq) datasets were obtained from The Cancer Genome Atlas[21]. Expression analyses were based on HTSeq count data generated using the Illumina HiSeq 2000 RNA Sequencing Version 2 platform. Raw counts were normalized with the "DESeq" package, which applies a negative binomial model [40]. Gene annotation was performed using the Bioconductor "AnnotationDbi" package (http://bioconductor.org/packages/AnnotationDbi/) to map Ensembl transcript IDs to gene symbols ($n = 25{,}228$). A secondary scaling normalization was implemented to adjust the mean gene expression of each sample to 1000 to mitigate batch effects. Cox proportional hazards regression was used to assess associations between gene expression and overall survival (OS). The "survival" R package (v2.38; http://CRAN.R-project.org/package=survival/) was used to compute log-rank P values, hazard ratios (HR), and 95% confidence intervals (CI). Kaplan–Meier survival curves were generated to visualize survival differences. To evaluate the prognostic significance of individual genes, patient samples were stratified by the lower (T1) and upper (T3) expression terciles of the biomarker. A follow-up cutoff of 48 months was applied. The only analytical restriction involved the AJCC lymph-node status. Under this criterion, the dataset comprised 407 patients. No further filtering was applied; consequently, the analysis did not adjust for HPV status, smoking history, or treatment.

Cell lines

FaDu and Cal-27 cell lines were grown in Dulbecco's Minimal Essential Medium (DMEM) supplemented with 10% fetal bovine serum (FBS) (Sigma), 1% penicillin-streptomycin (Corning), and 1% L-glutamine (Corning). Cells were cultured, adding CTX (Erbitux, Merck KgaA, Germany) at increasing concentrations for a few months, till the resistant cells were established and then maintained in culture at 20 µg/ml for FaDu and 50 µg/ml for Cal-27. Cells were cultured in 10 cm plastic Petri dishes in a humidified 37 °C incubator with 5% CO_2. The Bermekimab (BMK) was kindly provided by XBiotech in 2016, under a 2-year Material Transfer Agreement. Cells were routinely tested for *Mycoplasma* contamination by PCR.

Colony-forming assay

Cells were seeded in 12-well plates, 5000 cells/well for FaDu and 2000 cells/well for Cal-27, in 1 mL of full medium. Treatments were added the following day and refreshed after one week. After 10 days, the medium was removed, and cells were washed with PBS and fixed in 4% PFA for 20 min at room temperature. After washing with PBS, cells were stained with Crystal Violet 0.5% for 30 min and washed with water to remove excess dye. Pictures of each well were taken, and the covered area was measured using ImageJ software. The mean value for each treatment was calculated and reported as a percentage of the control.

Phasefocus Livecyte™

For Phasefocus Livecyte™ imaging, cells were seeded in 96-well plates, 2000 cells/well for FaDu and 1500 cells/well for Cal-27, in 100 µL of full medium and incubated overnight to allow cells' adhesion before starting Livecyte™ monitoring. Images of cells were taken at ×10 magnification every 30 min for a total of 3 days. Proliferation, random motility, and cell morphology parameters were computed by Phasefocus Livecyte™ software.

Antibody internalization assay

Cetuximab (Selleck Chemicals, A2000) was conjugated with pHrodo using the pHrodo iFL red microscale protein labeling kit (Thermo Scientific 36014) according to the manufacturer's instructions. Briefly, 1/10th volume of 1 M sodium bicarbonate solution was added to 1 mg/mL protein solution in PBS. 2 mM pHrodo was added to achieve a dye:protein molar ratio of 10. The reaction mixture was incubated at room temperature for 30 min and purified through a resin column. FaDu and FaDu-CXR cells were seeded in 96-well plates, 5000 cells/well in 100 mL of full medium and incubated overnight to allow cells' adhesion. Treatments were added the following day.

Phase contrast and red channel images (9 per well in duplicate for a total of 18 images per condition) were obtained on Incucyte S3 at an interval of 4 h at 37 °C for a total of 2 days. Relative internalization index was calculated according to the following formula:

$$Traffic\ index = \frac{red\ channel\ integrated\ intensity\ (per\ image)}{Cell\ area\ (per\ image)}$$

$$Relative\ internalization\ index = \frac{Traffic\ index}{I\max}$$

Where I_{max} is the maximum intensity value of CTX red channel.

Western blot

Cells were seeded in 6 cm plastic Petri dishes in 2 mL of 10% FBS medium. After overnight starvation, cells were treated according to the experiment. At the end point, cells were lysed using RIPA buffer supplemented with 1 mM Na_3VO_4 (Santa-Cruz Biotechnology, Dallas, USA) and a protease inhibitor cocktail (P8340, Sigma-Aldrich, St.Louise, Missouri, USA, 1:100). DC Protein Assay (Bio-Rad, Hercules, USA) was employed to assess protein concentration, using bovine serum albumin as the standard. Protein samples were resolved by sodium dodecyl sulfate (SDS)-poly-acrylamide gel electrophoresis and then transferred to nitrocellulose membranes (Amersham™ Protran™ Premium, GE Healthcare, USA). Blocking was performed by incubating membranes for 1 h with 5% BSA in TBS-T (0.1% Tween-20) and incubating O/N at 4 °C with primary antibodies. The following primary antibodies were used: anti-AKT rabbit polyclonal antibody (1:1000 dilution; #9272, Cell Signaling), anti-phospho-AKT (Ser473) (D9E) XP® rabbit monoclonal antibody (1:1000 dilution; #4060, Cell Signaling), anti-MAP Kinase activated (diphosphorylated ERK 1/2) mouse monoclonal antibody (1:10000 dilution; M8159, Sigma-Aldrich), anti-ERK 2 (D-2) mouse monoclonal antibody (1:1000 dilution; sc-1647, Santa Cruz Biotechnology), anti-EGF Receptor (D38B1) XP® rabbit monoclonal antibody (1:1000 dilution; #4267, Cell Signaling), anti-phospho-EGF Receptor (Tyr1068) (D7A5) XP® rabbit monoclonal antibody (1:1000 dilution; #3777, Cell Signaling), anti-alpha-Tubulin (B-7) mouse monoclonal antibody (1:1000 dilution; sc-5286, Santa Cruz Biotechnology), anti-GAPDH rabbit polyclonal antibody (1:10.000 dilution; G9545, Sigma-Aldrich), anti-IL-1RI (H-8) mouse monoclonal antibody (1:1000 dilution; sc-393998, Santa Cruz Biotechnology). Membranes were then incubated for 1 h with horseradish peroxidase-conjugated secondary antibodies (Peroxidase AffiniPure™ Goat Anti-Rabbit IgG (H + L), 111-035-003, and Peroxidase AffiniPure™ Goat Anti-Mouse IgG (H + L), 115-035-003, Jackson ImmunoResearch Laboratories) and protein bands were detected by chemiluminescence (Clarity Western ECL Substrate, Bio-Rad). Images were acquired and analyzed using ImageLab software.

3D spheroid assay

For spheroid formation assays, 96-well plates were covered with a layer of sterile agar 1.8% (~60 µl for each well). 20,000 cells for each well were seeded in 100 µl of 10% FBS medium. The day after, photos for time 0 were taken at ×4 magnification, and then treatments were added according to the experiment. After 96 h, pictures of the spheroids were taken as described above. Masks of each spheroid were obtained with ImageJ software and then used to estimate the spheroids' volume with ReViSP v2.3 software. The software was also employed to obtain the 3D rendering of FaDu spheroids. Data were analyzed by subtracting the initial volume ($t0$) from the final volume ($t96$) to obtain the absolute change. Then, the percent relative change was determined by applying the formula: Relative Percent Change = ($t0$ Volume − $t96$ Volume + $t0$ Volume) × 100. This value represented the difference, whether positive or negative, from the initial value.

Tissues sections and hematoxylin-eosin staining

Spheroids from 3D culture and lungs from in vivo experiment were collected and formalin-fixed for 24 h. After PBS washing, spheroids were dehydrated in 70%, 90%, and 100% concentration of ethanol and processed with a clearing solution (Toluene) with a microwave processor (Milestone). After drying, samples were paraffin-embedded, followed by microtome cutting (Leica, RM2125 RTS). Three-micrometer-thick sections were put overnight at 38 °C in a dry stove. Section was dewaxed (Toluene) and rehydrated at decreasing concentration of ethanol (100%, 100%, 95%, and 70%) and washed with water. Hematoxylin-eosin staining was performed to assess the integrity of the section. Section was dehydrated as above and passed two times in toluene for 3 min. Cover slip was applied using DXP mounting media and left to dry. Spheroid photos were taken at ×20 magnification (Leica DM750), and lung images were acquired with SLIDEVIEW VS200 (Olympus).

Immunohistochemistry

Spheroids' immunohistochemistry was performed using a Bench-Mark ULTRA automated immunostainer (Ventana Medical Systems-Roche Diagnostics, Switzerland). The following antibodies were used: E-cadherin (clone 36, mouse monoclonal primary antibody), Vimentin (clone V9, primary antibody) and Ki67 (clone 30-9, rabbit monoclonal primary antibody). Photos were taken at ×20 magnification (Leica DM750). Lung tissues from in vivo experiments were stained using an automated immunostainer (DISCOVERY ULTRA, Roche). Sections were incubated with a rabbit monoclonal anti-cytokeratin 14 antibody (clone SP53, Roche) at 2.89 µg/mL. Signal detection was performed using the DISCOVERY OmniMap anti-Rb HRP (RUO) detection system with DAB as chromogen. Slides were counterstained with Hematoxylin II and Bluing Reagent (Roche). Whole-slide images were acquired using the OlyVIA VS200 Slidescan.

Immunofluorescence

Cells were seeded into glass coverslips placed in 24-well plates, 4×10^4 cells/well, in 500 µL of full medium and incubated overnight to allow cells' adhesion. Treatments were added the following day according to the experiment. At end point, cells were washed with PBS and fixed with 4% PFA for 20 min. Samples were blocked with 1% BSA for 30 min and incubated overnight at room temperature in a humidified chamber with anti-EGFR (sc-101; Santa Cruz Biotechnology) or anti-phospho-Histone H2A.X (Ser139) (sc-517348; Santa Cruz Biotechnology) primary antibodies. After washing, cells were incubated for 1 h at room temperature with Alexa Fluor 594 AffiniPure Goat Anti-Mouse IgG (H + L) secondary antibody (115-585-003; Jackson ImmunoResearch). Nuclei and F-actin were counterstained with DAPI (#D9542; Sigma-Aldrich) and phalloidin (#A12379; Thermo Fisher Scientific) for 30 min. Coverslips were mounted using a glycerol: PBS (6:4) mounting medium. Imaging was performed using the Olympus BH-2 CCD microscope. Representative images were acquired using the IXplore IX83 SpinSR spinning disk confocal microscope (Olympus/Evident).

For 3D cultures, FaDu and FaDu-CXR spheroids were formalin-fixed and paraffin-embedded (FFPE). Sections were dewaxed (Toluene) and dehydrated through a graded ethanol series (100%, 100%, 95%, and 70%) and subjected to antigen retrieval in EDTA buffer. Samples were permeabilized with 0.2% Triton X-100 and blocked in 1% BSA for 1 h at room temperature. Sections were incubated overnight at 4 °C in a humidified chamber with anti-phospho-Histone H2A.X (Ser139) antibody (sc-517348; Santa Cruz Biotechnology), followed by a 1 h incubation with Alexa Fluor 594 AffiniPure Goat Anti-Mouse IgG (H + L) secondary antibody (115-585-003; Jackson ImmunoResearch). Nuclei were counterstained with DAPI (30 min; Sigma-Aldrich). Whole-slide images were acquired using the OlyVIA VS200 Slidescan system.

In vivo experiment

All animal procedures were approved by the Institutional Animal Care and Use Committee (CoBA) of the University of Bologna and authorized by the

Italian Ministry of Health (Directorate General for Animal Health and Veterinary Medicines; letter 663-2022-PR). Experiments were conducted in accordance with national legislation (Legislative Decree 26/2014). Female Athymic Nude-Fox1nu/nu mice (7 weeks old) were housed under controlled conditions (20–25 °C; 40–60% humidity; 12-h light/dark cycle) with ad libitum access to food and water. Animals were acclimatized for at least one week prior to experimental procedures.

Experimental lung metastasis was established by tail vein injection of 2×10^6 FaDu-CXR cells suspended in 150 µL PBS. Mice were randomly assigned to two groups using simple randomization: CTX alone (100 mg/injection; $n = 8$) or CTX combined with ANA (10 mg/kg; $n = 9$). Treatment started 5 days after cell injection. CTX was administered intraperitoneally (i.p.) twice weekly (every 3–4 days), while ANA was administered i.p. daily for the duration of the study. Animals were monitored regularly for clinical signs of distress, including weight loss, lethargy, and hunched posture. Mice were euthanized at 6 weeks post-injection or earlier upon reaching predefined humane endpoints. Euthanasia was performed by isoflurane overdose followed by cervical dislocation. Lungs were harvested for metastasis evaluation by quantitative real-time PCR (qPCR), hematoxylin-eosin staining, and immunohistochemistry. In a second replicate, mice were treated as described above for 4 weeks (CTX, $n = 6$; CTX + ANA, $n = 7$), and lung tissues were collected for qPCR analysis.

RNA isolation and qPCR

FaDu and FaDu-CXR cells were seeded in 6 cm plastic Petri dishes, 6×10^5 cells for each dish, in 2 mL of 10% FBS medium. After overnight starvation, cells were treated according to the experiment. At end point, total RNA was extracted from cells with QIAzol® Lysis Reagent (QIAGEN, Venlo, Netherlands) following manufacturer's instructions. Reverse transcription (RT) was carried out using High-Capacity cDNA Reverse Transcription Kit (Applied Biosystems™). qRT-PCR analyses were then performed on cDNA using the SsoFast EvaGreen Supermix (Bio-Rad, Hercules, USA) in a C1000 Touch™ Thermal Cycler (Bio-Rad, California, USA) coupled with the CFX96TM Real-Time PCR Detection System (Bio-Rad). qRT-PCR analysis was performed as ΔCq (Quantification Cycle). ΔCq were normalized on the expression of β_2-microglobulin (B2M) housekeeping gene.

Primer list:

TARGET TRANSCRIPT	5'→3' SEQUENCE	SOURCE
IL-1R	FW:TGCGTGGTAAGAAATTCATC	Sigma-Aldrich
	RW:ACTCCATATAAGGGCACAC	Sigma-Aldrich
IL-1α	FW:AGAGGAAGAAATCATCAAGC	Sigma-Aldrich
	RW:TTATACTTTGATTGAGGGCG	Sigma-Aldrich
IL-1β	FW:CTAAACAGATGAAGTGCTCC	Sigma-Aldrich
	RW:GGTCATTCTCCTGGAAGG	Sigma-Aldrich
IL-6	FW: AAGATTCCAAAGATGTAGCC	Sigma-Aldrich
	RW: ACATGTCTCCTTTCTCAGG	Sigma-Aldrich
IL-8	FW:CGGAAGGAACCATCTCACTG	Sigma-Aldrich
	RW:AGCACTCCTTGGCAAAACTG	Sigma-Aldrich
SNAI	FW:CTCTAATCCAGAGTTTACCTTC	Sigma-Aldrich
	RW:GACAGAGTCCCAGATGAG	Sigma-Aldrich
B2M	FW:TGCCTGCCGTGTGAACCATGT	Sigma-Aldrich
	RW:TGCGGCATCTTCAAACCTCCATGA	Sigma-Aldrich
Murine GAPDH	FW:TCACCACCATGGAGAAGGC	Sigma-Aldrich
	RW:GCTAAGCAGTTGGTGGTGCA	Sigma-Aldrich

Gelatin degradation assay

Gelatin degradation assay was performed by coating glass coverslips with Oregon green-488 conjugated gelatin from pig skin (InvitrogenTM, Waltham, USA) diluted to a final concentration of 0.2 mg/mL in PBS + sucrose 2%. After coating solidification, gelatin was treated for 15′ on ice with cold glutaraldehyde 0.5% in PBS and then with NaBH4 5 mg/mL in PBS for 3′ at room temperature. Coated coverslips were stored at +4 °C in PBS + P/S 1:50 protected from light until seeding day. FaDu and FaDu-CXR cells (4×10^4 cells/well) were seeded in 800 µl of 10% FBS medium. After cells adhesion, treatments were added for 36 h. The coverslips were then fixed with PFA 4% for 15′, blocked for 30′ with BSA3% + 0.1 Triton X-100 and finally stained with Phalloidin-TRITC (Sigma Aldrich, St.Louise, Missouri, USA) and DAPI (Sigma Aldrich, St.Louise, Missouri, USA) diluted in BSA 0.3% + 0.1 Triton X-100 for 1 h. Imaging was performed using the Olympus BH-2 CCD microscope. Images were analyzed using ImageJ software and degradation was measured in the green channel in terms of area of degraded gelatin (without green fluorescence) normalized on nuclei number (DAPI).

Statistical analysis

The statistical analyses were performed by using Prism version 9 (GraphPad Software, Inc). T-test, one-way ANOVA and two-way ANOVA were used to test the significance of the assays. The details of the applied statistical test are reported in the figure legends. *P value < 0.05; **P value < 0.01; ***P value < 0.001; ****P value < 0.0001.

Data availability

All data generated or analyzed during this study are available in the manuscript and supplementary materials. Further inquiries can be directed to the corresponding authors.

Received: 31 October 2025; Accepted: 16 March 2026;
Published online: 08 April 2026

References

1. Bray, F. et al. Global cancer statistics 2022: GLOBOCAN estimates of incidence and mortality worldwide for 36 cancers in 185 countries. *CA Cancer J. Clin.* **74**, 229–263 (2024).
2. Zhu, X. et al. Prognostic role of epidermal growth factor receptor in head and neck cancer: a meta-analysis. *J. Surg. Oncol.* **108**, 387–397 (2013).
3. Solomon, B., Young, R. J. & Rischin, D. Head and neck squamous cell carcinoma: genomics and emerging biomarkers for immunomodulatory cancer treatments. *Semin. Cancer Biol.* **52**, 228–240 (2018).
4. Almadori, G. et al. Prognostic significance and clinical relevance of the expression of the HER family of type I receptor tyrosine kinases in human laryngeal squamous cell carcinoma. *Eur. J. Cancer* **46**, 1144–1152 (2010).
5. Bonner, J. A. et al. Radiotherapy plus cetuximab for squamous-cell carcinoma of the head and neck. *N. Engl. J. Med.* **354**, 567–578 (2006).
6. Alsahafi, E. et al. Clinical update on head and neck cancer: molecular biology and ongoing challenges. *Cell Death Dis.* **10**, 1–17 (2019).
7. Ferris, R. L. et al. Nivolumab for recurrent squamous-cell carcinoma of the head and neck. *N. Engl. J. Med.* **375**, 1856–1867 (2016).
8. Kao, H. F., Huang, H. C., Liao, B. C. & Hong, R. L. Short-course pembrolizumab and continuous afatinib therapy for recurrent or metastatic head and neck squamous cell carcinoma: a real-world data analysis. *BMC Cancer* **22**, 1–9 (2022).
9. Gelfo, V. et al. Roles of IL-1 in cancer: from tumor progression to resistance to targeted therapies. *Int. J. Mol. Sci.* **21**, 1–14 (2020).
10. Gelfo, V. et al. A novel role for the interleukin-1 receptor axis in resistance to anti-EGFR therapy. *Cancers* **10**, 355 (2018).
11. Romaniello, D. et al. Senescence-associated reprogramming induced by interleukin-1 impairs response to EGFR neutralization. *Cell. Mol. Biol. Lett*. https://doi.org/10.1186/S11658-022-00319-7.
12. Rao, S. K. et al. Pro-inflammatory genes as biomarkers and therapeutic targets in oral squamous cell carcinoma. *J. Biol. Chem.* **285**, 32512–32521 (2010).

13. Goertzen, C. et al. Oral inflammation promotes oral squamous cell carcinoma invasion. *Oncotarget* **9**, 29047–29063 (2018).
14. Al-Sahaf, S. et al. Increased abundance of tumour-associated neutrophils in HPV-negative compared to HPV-positive oropharyngeal squamous cell carcinoma is mediated by IL-1R signalling. *Front. Oral Health* https://doi.org/10.3389/FROH.2021.604565.
15. Lewis, A. M., Varghese, S., Xu, H. & Alexander, H. R. Interleukin-1 and cancer progression: the emerging role of interleukin-1 receptor antagonist as a novel therapeutic agent in cancer treatment. *J. Transl. Med*. https://doi.org/10.1186/1479-5876-4-48.
16. Lee, C. H. et al. IL-1β promotes malignant transformation and tumor aggressiveness in oral cancer. *J. Cell. Physiol.* **230**, 875–884, https://doi.org/10.1002/JCP.24816 (2015).
17. Niklander, S. E., Murdoch, C. & Hunter, K. D. IL-1/IL-1R signaling in head and neck cancer, *Front. Oral Health* https://doi.org/10.3389/FROH.2021.722676.
18. Dinarello, C. A. Why not treat human cancer with interleukin-1 blockade? *Cancer Metastasis Rev.* **29**, 317–329 (2010).
19. León, X. et al. Expression of IL-1α correlates with distant metastasis in patients with head and neck squamous cell carcinoma. *Oncotarget* **6**, 37398–37409 (2015).
20. Győrffy, B. Integrated analysis of public datasets for the discovery and validation of survival-associated genes in solid tumors. *Innovation* https://doi.org/10.1016/j.xinn.2024.100625.
21. Lawrence, M. S. et al. Comprehensive genomic characterization of head and neck squamous cell carcinomas. *Nature* **517**, 576–582 (2015).
22. Oren, Y. et al. Cycling cancer persister cells arise from lineages with distinct programs. *Nature* **596**, 576–582 (2021).
23. Espinosa-Cotton, M. et al. Interleukin-1 alpha increases anti-tumor efficacy of cetuximab in head and neck squamous cell carcinoma. *J. Immunother. Cancer* **7**, 79 (2019).
24. Russo, M. et al. Adaptive mutability of colorectal cancers in response to targeted therapies. *Science* **366**, 1473–1480 (2019).
25. Elmusrati, A., Wang, J. & Wang, C. Y. Tumor microenvironment and immune evasion in head and neck squamous cell carcinoma. *Int. J. Oral. Sci.* **13**, 24 (2021).
26. Rajan, A. et al. Impact of nuclear interleukin-1 alpha and EGFR expression on recurrence and survival outcomes in oral squamous cell carcinomas. *J. Oncol*. https://doi.org/10.1155/2019/5859680.
27. Mair, F. et al. Extricating human tumour immune alterations from tissue inflammation. *Nature* **605**, 728–735 (2022).
28. Sacco, A. G. et al. Pembrolizumab plus cetuximab in patients with recurrent or metastatic head and neck squamous cell carcinoma: an open-label, multi-arm, non-randomised, multicentre, phase 2 trial. *Lancet Oncol.* **22**, 883–892 (2021).
29. Koch, A. T., Love-Homan, L., Espinosa-Cotton, M., Stanam, A. & Simons, A. L. MyD88-dependent signaling decreases the antitumor efficacy of epidermal growth factor receptor inhibition in head and neck cancer cells. *Cancer Res.* **75**, 1657–1667 (2015).
30. Espinosa-Cotton, M. et al. A preliminary analysis of interleukin-1 ligands as potential predictive biomarkers of response to cetuximab. *Biomark. Res.* **7**, 14 (2019).
31. Stanam, A. et al. Interleukin-1 blockade overcomes erlotinib resistance in head and neck squamous cell carcinoma. *Oncotarget* **7**, 76087–76100 (2016).
32. Pu, Y. et al. Drug-tolerant persister cells in cancer: the cutting edges and future directions. *Nat. Rev. Clin. Oncol.* **20**, 799–813 (2023).
33. Liu, J. Y. et al. Cells exhibiting strong p16 INK4a promoter activation in vivo display features of senescence. *Proc. Natl. Acad. Sci. USA* **116**, 2603–2611 (2019).
34. Feringa, F. M. et al. Persistent repair intermediates induce senescence. *Nat. Commun.* **9**, 1–10 (2018).
35. Pezone, A. et al. Inflammation and DNA damage: cause, effect or both. *Nat. Rev. Rheumatol.* **19**, 200–211 (2023).
36. Russo, M. et al. Cancer drug-tolerant persister cells: from biological questions to clinical opportunities. *Nat. Rev. Cancer* https://doi.org/10.1038/S41568-024-00737-Z.
37. Nastasi, C., Mannarino, L. & D'incalci, M. DNA damage response and immune defense. *Int. J. Mol. Sci.* **21**, 7504 (2020).
38. Yang, J. et al. Aspirin prevents metastasis by limiting platelet TXA2 suppression of T cell immunity. *Nature* **640**, 1052–1061 (2025).
39. Chia, S.B. et al. Respiratory viral infections awaken metastatic breast cancer cells in lungs. *Nature* **645**, 496–506 (2025).
40. Anders, S. & Huber, W. Differential expression analysis for sequence count data, *Genome Biol*. https://doi.org/10.1186/gb-2010-11-10-r106.

Acknowledgements

The research leading to these results has received funding by the AIRC IG 2024, Rif. 28760 to M.L. and from the Italian Ministry of Health, RC-2025-2794605 project to A.A. and M.L. Moreover, this research was supported by the Italian Ministry of University and Research under PRIN-PNRR2022 - to M.L. The views and opinions expressed are those of the authors only and do not necessarily reflect those of the European Union or the European Commission. Neither the European Union nor the European Commission can be held responsible for them. During the preparation of this work the authors used ChatGPT to improve language and readability. After using this tool, the authors reviewed and edited the content as needed and take full responsibility for the content of the publication.

Author contributions

F.P., F.B., V.G., A.M., M.S. and M.M. performed and analyzed the in vitro experiments, execution, and interpretation of the cellular assays. C.G. and D.R. carried out the in vivo studies, including experimental procedures, data collection, and subsequent analysis. B.G. conducted the bioinformatic analyses of patient datasets. F.P. and M.L. were the major contributors in the design of the experiments and the writing of the manuscript, drafting and organizing the text. G.Q. and F.A. carried out IHC staining and analysis. D.M.F., C.M., G.D., F.F., P.C.-R., M.S. and A.A. critically revised the manuscript, providing intellectual input and improving the clarity of the work. All authors read and approved the final version of the manuscript.

Competing interests

Corresponding author M.L. is an Associate Editor, and the co-author P.C.-R. is a Deputy Editor of npj Precision Oncology. They were not involved in the journal's review of this manuscript. The other authors have no competing interests to declare.

Additional information

Supplementary information The online version contains supplementary material available at https://doi.org/10.1038/s41698-026-01389-y.

Correspondence and requests for materials should be addressed to Michela Sgarzi or Mattia Lauriola.